



## Utility of thermal image sharpening for monitoring field-scale evapotranspiration over rainfed and irrigated agricultural regions

Nurit Agam,<sup>1</sup> William P. Kustas,<sup>1</sup> Martha C. Anderson,<sup>1</sup> Fuqin Li,<sup>1</sup> and Paul D. Colaizzi<sup>2</sup>

Received 2 October 2007; revised 23 October 2007; accepted 13 December 2007; published 19 January 2008.

[1] The utility of a thermal image sharpening algorithm (TsHARP) in providing fine resolution land surface temperature data to a Two-Source-Model for mapping evapotranspiration (ET) was examined over two agricultural regions in the U.S. One site is in a rainfed corn and soybean production region in central Iowa. The other lies within the Texas High Plains, an irrigated agricultural area. It is concluded that in the absence of fine (sub-field scale) resolution thermal data, TsHARP provides an important tool for monitoring ET over rainfed agricultural areas. In contrast, over irrigated regions, TsHARP applied to kilometer-resolution thermal imagery is unable to provide accurate fine resolution land surface temperature due to significant sub-pixel moisture variations that are not captured in the sharpening procedure. Consequently, reliable estimation of ET and crop stress requires thermal imagery acquired at high spatial resolution, resolving the dominant length-scales of moisture variability present within the landscape. **Citation:** Agam, N., W. P. Kustas, M. C. Anderson, F. Li, and P. D. Colaizzi (2008), Utility of thermal image sharpening for monitoring field-scale evapotranspiration over rainfed and irrigated agricultural regions, *Geophys. Res. Lett.*, 35, L02402, doi:10.1029/2007GL032195.

### 1. Introduction

[2] Over the last several decades, there has been a major effort to develop methods for deriving spatially-distributed evapotranspiration (ET) maps over landscapes by using remote sensing imagery in the visible–near-infrared (VIS/NIR) and the thermal infrared (TIR) bands in surface energy balance models [Diak *et al.*, 2004]. The spatial resolution of the resulting ET maps is determined by the spatial resolution of the coarsest input, and the temporal frequency is determined by the revisit time of the acquiring satellite system. For water management applications and other agricultural purposes, ET maps would be optimally produced daily at fine spatial resolution (<100 m). However, a tradeoff exists between the spatial and temporal resolutions of current remote sensing systems, such that they typically have either high-spatial/low-temporal or low-spatial/high-temporal resolution. This tradeoff is particularly significant for satellite-based thermal imaging instruments, which have 2–10 times coarser resolution than do co-located VIS/NIR sensors.

[3] With the currently available satellite systems, several strategies can be applied for mapping ET over agricultural areas. The first is to derive fine resolution (60–120 m) maps at ca. monthly intervals using Landsat TIR data. This option provides adequate within-field resolution, and provides the most reliable estimates of field-scale ET. The shortcomings of this method are the long time-lag between image acquisitions and the uncertainty as to whether thermal imaging will be continued on the next generation Landsat satellites. Alternatively, coarser resolution (1 km) ET maps can be generated at ~daily time steps using, for example, the Moderate Resolution Imaging Spectrometer (MODIS) on board the Terra/Aqua satellites [Nishida *et al.*, 2003]. While providing better temporal coverage, 1 km-scale maps cannot capture within-field variations, which are important for agricultural management at the field and farm level. A third strategy utilizes the functional relationship between the spaceborne-derived surface temperature and vegetation indices to sharpen the 1 km MODIS TIR imagery to the resolution of the MODIS VIS/NIR bands (250 m), deriving near daily ET maps at scales marginally resolving the typical field size (TsHARP) [Kustas *et al.*, 2003; Agam *et al.*, 2007a, 2007b]. Provided that the sharpening algorithm reasonably reproduces the actual land surface temperature (LST) distributions at the target resolution, this approach may provide the most optimal means for deriving routine remotely-sensed ET maps at field scale.

[4] In this study, a Two-Source-Model (TSM) of surface energy balance was used to derive ET maps using TIR data at different spatial resolutions. Detailed description of the model principles and formulation are given by Norman *et al.* [1995] and Kustas and Norman [1999a, 1999b, 2000]. Briefly, the TSM is a land-surface parameterization of the radiation and turbulent energy exchanges between the soil, vegetation and lower atmosphere. Given an estimate of fractional vegetation cover, the TSM partitions the surface temperature and energy/water fluxes into soil and canopy contributions, and has a built-in mechanism for detecting thermal signatures of stress in the soil and canopy.

[5] The utility of TsHARP for TSM flux evaluations was examined over two agricultural regions in the U.S.: a rainfed corn and soybean production region in central Iowa, and an irrigated agricultural area in the Texas Panhandle. The goal was to estimate errors in ET incurred by using sharpened thermal imagery in place of imagery acquired at fine-scale native resolution. Although other TIR-based energy balance models may have somewhat differing sensitivity to errors in the input surface temperature field, the TSM is considered here as one possible mapping from LST to ET space to give a qualitative estimate of the impacts of

<sup>1</sup>Hydrology and Remote Sensing Laboratory, Agricultural Research Service, U.S. Department of Agriculture, Beltsville, Maryland, USA.

<sup>2</sup>Conservation and Production Research Laboratory, Agricultural Research Service, U.S. Department of Agriculture, Bushland, Texas, USA.

image resolution on practical utility in water management applications in these two representative agricultural areas.

## 2. Methodology

### 2.1. Sharpening Algorithm

[6] The TsHARP algorithm, originally developed by *Kustas et al.* [2003] and refined by *Agam et al.* [2007a], uses high-resolution information of vegetation cover fraction, derived from VIS/NIR data in the form of the Normalized Difference Vegetation Index (NDVI), to sharpen temperature maps from coarser-resolution thermal bands. The implicit assumption is that fractional vegetation cover, which is related to NDVI, is one of the primary factors affecting LST variations across a given scene. Operationally, the NDVI data are aggregated to the coarser thermal resolution and a least-squares regression is performed between the radiometric temperature and a function  $f(\text{NDVI})$  that is related to fractional vegetation cover. The regression parameters are then applied to the NDVI data at their finer native resolution. Finally, this base map is re-aggregated to the coarse thermal resolution and differenced with the observed temperature field. These coarse-scale residuals represent variability in temperature driven by factors other than vegetation cover fraction (for example, soil moisture variations). The residuals are added back into the high-resolution base map, ensuring that the observed temperature field will be recovered through re-aggregation.

### 2.2. Study Area and Satellite Imagery

#### 2.2.1. Walnut Creek Watershed (WCW), Iowa—Rainfed Agriculture

[7] A grid-box  $\sim 10$  km north–south by 30 km east–west, encompassing the Walnut Creek Watershed (WCW; centered at  $34^{\circ}44'N$   $101^{\circ}37'W$ ) was subset from a Landsat ETM+ scene acquired on July 1, 2002. The WCW lies within the upper Midwest corn and soybean production region in central Iowa, characterized mainly by rainfed agriculture. In this humid region, the most rapid growth in corn and soybean crops is observed in June–July. During this period, rainfall events are often in the form of thunderstorms, providing brief and intense showers [*Hatfield et al.*, 1999]. The July 1 scene was acquired following a  $\sim 10$  day dry-down interval, resulting in strong variability in soil moisture and crop conditions.

#### 2.2.2. Texas High Plains (THP), Texas—Irrigated Agriculture

[8] A subset ( $\sim 10$  km north–south by 30 km east–west, centered at  $34^{\circ}37'N$ ,  $102^{\circ}53'W$ ) of a full Landsat ETM+ scene (acquired on September 22, 2002) overlying the northern part of the Texas–New Mexico state border was used in this study. This area is part of the Southern High Plains, within the larger Great Plains of the western United States, and is mostly comprised of irrigated agricultural fields [*Colaizzi et al.*, 2006]. In the Texas High Plains (THP) region, September is a relatively dry month, during which the cotton crops are reaching maturity and are thus unlikely to be irrigated, while emerging winter wheat crops are typically receiving irrigation. The study area therefore exhibited large variability in vegetation cover and moisture conditions (due to irrigation) at the time of image acquisition. However, due to seasonality, net radiation and ET are

expected to be lower on average for the late September THP scene than for the early July WCW scene described above.

### 2.3. Simulated Scaling Experiment

#### 2.3.1. Pre-processing

[9] The two Landsat ETM+ scenes provided VIS/NIR and TIR data at 30 and 60 m native resolution, respectively. The scenes were atmospherically corrected using MODTRAN [*Berk et al.*, 1998]. The brightness temperatures were then corrected for emissivity effects using a fractional cover mixture model [*Sobrino et al.*, 2001] to retrieve surface radiometric temperature, following the procedure described by *Li et al.* [2004].

#### 2.3.2. Data Scaling

[10] Four spatial resolutions were examined in this study: 60, 120, and 240 (hereafter the “finer” or “target” resolutions), and 960 m (hereafter the “coarse” resolution). In order to avoid errors introduced by inter-sensor comparisons caused by differences in view angle, pixel registration, and overpass time, the Landsat ETM+ VIS/NIR and TIR bands were spatially aggregated to simulate MODIS-resolution data, sharpened, and then validated with respect to ETM+ TIR distributions at the finer resolutions. Note that unless explicitly mentioned, the described processes were applied similarly to both sites.

##### 2.3.2.1. VIS/NIR Data

[11] During the Soil Moisture Atmosphere Coupling Experiment (SMACEX) [*Kustas et al.*, 2005], extensive sampling of vegetation cover fraction and canopy architecture was conducted over the WCW [*Anderson et al.*, 2004] and a supervised landcover classification at 30-m resolution was performed [*Doraiswamy et al.*, 2004]. Due to a lack of ground-truth data over the THP, a 30-m landuse map for the Texas scene was obtained by classifying the study area into general landcover categories of agricultural land and natural vegetation using a semi-supervised classification technique [*Agam et al.*, in press].

[12] Following *Anderson et al.* [2004], who demonstrated near-linear scaling in VI, NDVI was aggregated to resolutions of 60, 120, 240, and 960 m and then cover fraction was computed from NDVI at these resolutions. Canopy height (affecting model surface roughness) was assigned to the target grids using the “mixed class” technique described by *Anderson et al.* [2004, 2007]. Accordingly, the derived fluxes represent outputs one might obtain in practice, using 30 m landuse maps (available, e.g., from the National Land Cover Dataset [*Homer et al.*, 2004]) in conjunction with NDVI data available at the target resolution.

##### 2.3.2.2. TIR Data

[13] Simulated TIR images at 120, 240 and 960 m resolutions were generated by converting original brightness temperature data at 60 m to radiance values using the Stephan-Boltzmann law with an exponent of 4 [*Becker and Li*, 1990; *Norman and Becker*, 1995], computing an average radiance over the coarser pixel area, and then re-converting to brightness temperature. The sharpening algorithm was then applied to the coarse 960 m TIR field to create sharpened temperature fields at each of the finer resolutions.

##### 2.3.2.3. Weather Station Data

[14] For both sites, meteorological data used by the TSM, consisting primarily of 30-min average wind speed, air

**Table 1.** Statistical Comparison of Flux Maps Generated With the TsHARP and UniFlux Methods and Reference Flux Fields at 60, 120, and 240 m Resolution for Walnut Creek Watershed (WCW; Rainfed Agriculture) and Texas High Plains (THP; Irrigated Agriculture) Study Sites<sup>a</sup>

| Res., m | Method  | WCW - Rainfed Agriculture                     |                           |                    |                |                | THP - Irrigated Agriculture                   |                           |                    |                |                |
|---------|---------|---|---------------------------|--------------------|----------------|----------------|---|---------------------------|--------------------|----------------|----------------|
|         |         | Mean (STD), <sup>b</sup><br>W m <sup>-2</sup> | MAE,<br>W m <sup>-2</sup> | Regression Results |                |                | Mean (STD), <sup>b</sup><br>W m <sup>-2</sup> | MAE,<br>W m <sup>-2</sup> | Regression Results |                |                |
|         |         |   |                           | a <sub>0</sub>     | a <sub>1</sub> | r <sup>2</sup> |   |                           | a <sub>0</sub>     | a <sub>1</sub> | r <sup>2</sup> |
|         |         |   |                           |                    |                |                |   |                           |                    |                |                |
|         |         |   |                           |                    |                | <i>Rn</i>      |   |                           |                    |                |                |
| 60      | TsHARP  | 626 (19)                                      | 6                         | 135                | 0.79           | 0.69           | 455 (22)                                      | 6                         | 44                 | 0.90           | 0.87           |
| 60      | uniFlux | 626 (19)                                      | 13                        | 469                | 0.26           | 0.14           | 455 (22)                                      | 15                        | 325                | 0.29           | 0.28           |
| 120     | TsHARP  | 626 (18)                                      | 5                         | 83                 | 0.87           | 0.84           | 456 (21)                                      | 5                         | 46                 | 0.90           | 0.88           |
| 120     | uniFlux | 626 (18)                                      | 13                        | 536                | 0.15           | 0.47           | 456 (21)                                      | 14                        | 375                | 0.34           | 0.33           |
| 240     | TsHARP  | 627 (16)                                      | 4                         | 78                 | 0.88           | 0.89           | 456 (20)                                      | 4                         | 40                 | 0.91           | 0.90           |
| 240     | uniFlux | 627 (16)                                      | 10                        | 389                | 0.38           | 0.37           | 456 (20)                                      | 12                        | 277                | 0.40           | 0.38           |
|         |         |   |                           |                    |                | <i>G</i>       |   |                           |                    |                |                |
| 60      | TsHARP  | 96 (38)                                       | 4                         | 3                  | 0.97           | 0.97           | 89 (20)                                       | 2                         | 3                  | 0.97           | 0.97           |
| 60      | uniFlux | 96 (38)                                       | 18                        | 74                 | 0.27           | 0.26           | 89 (20)                                       | 14                        | 67                 | 0.25           | 0.22           |
| 120     | TsHARP  | 96 (34)                                       | 3                         | 1                  | 0.99           | 0.97           | 89 (19)                                       | 2                         | 2                  | 0.98           | 0.98           |
| 120     | uniFlux | 96 (34)                                       | 16                        | 64                 | 0.31           | 0.32           | 89 (19)                                       | 12                        | 63                 | 0.29           | 0.28           |
| 240     | TsHARP  | 97 (29)                                       | 2                         | 0                  | 1.00           | 0.98           | 90 (18)                                       | 2                         | 2                  | 0.98           | 0.98           |
| 240     | uniFlux | 97 (29)                                       | 13                        | 52                 | 0.41           | 0.41           | 90 (18)                                       | 11                        | 60                 | 0.34           | 0.33           |
|         |         |   |                           |                    |                | <i>H</i>       |   |                           |                    |                |                |
| 60      | TsHARP  | 131 (72)                                      | 30                        | 59                 | 0.48           | 0.42           | 196 (46)                                      | 28                        | 134                | 0.27           | 0.22           |
| 60      | uniFlux | 131 (72)                                      | 38                        | 109                | 0.26           | 0.21           | 196 (46)                                      | 29                        | 162                | 0.14           | 0.16           |
| 120     | TsHARP  | 126 (61)                                      | 24                        | 48                 | 0.57           | 0.56           | 195 (39)                                      | 24                        | 125                | 0.32           | 0.25           |
| 120     | uniFlux | 126 (61)                                      | 40                        | 105                | 0.27           | 0.22           | 195 (39)                                      | 26                        | 151                | 0.20           | 0.22           |
| 240     | TsHARP  | 124 (70)                                      | 20                        | 42                 | 0.63           | 0.65           | 193 (43)                                      | 18                        | 112                | 0.39           | 0.30           |
| 240     | uniFlux | 124 (70)                                      | 28                        | 94                 | 0.32           | 0.33           | 193 (43)                                      | 18                        | 134                | 0.29           | 0.30           |
|         |         |   |                           |                    |                | <i>E</i>       |   |                           |                    |                |                |
| 60      | TsHARP  | 407 (91)                                      | 32                        | 118                | 0.74           | 0.72           | 170 (52)                                      | 31                        | 98                 | 0.48           | 0.32           |
| 60      | uniFlux | 407 (91)                                      | 61                        | 334                | 0.21           | 0.21           | 170 (52)                                      | 34                        | 129                | 0.28           | 0.24           |
| 120     | TsHARP  | 405 (81)                                      | 26                        | 103                | 0.77           | 0.81           | 172 (48)                                      | 27                        | 86                 | 0.54           | 0.40           |
| 120     | uniFlux | 405 (81)                                      | 63                        | 321                | 0.23           | 0.25           | 172 (48)                                      | 30                        | 115                | 0.33           | 0.29           |
| 240     | TsHARP  | 407 (48)                                      | 21                        | 95                 | 0.79           | 0.86           | 173 (32)                                      | 21                        | 65                 | 0.65           | 0.53           |
| 240     | uniFlux | 407 (48)                                      | 48                        | 300                | 0.29           | 0.29           | 173 (32)                                      | 26                        | 107                | 0.40           | 0.37           |

<sup>a</sup>MAE stands for Mean Absolute Error and the regression parameters describe the best-fit line  $F_{\text{mod}} = a_0 + a_1 F_{\text{ref}}$ , where  $F_{\text{mod}}$  and  $F_{\text{ref}}$  are the sharpened and reference fluxes, respectively.

<sup>b</sup>Mean and standard deviations were computed from the reference flux maps.

temperature, relative humidity, and solar radiation, were obtained from local weather stations ~2 m above the canopy layer and applied uniformly across the images.

### 2.3.3. Generation of Multi-scale Flux Maps

[15] For each of the sharpening target resolutions three different types of flux maps have been generated and intercompared:

#### 2.3.3.1. Reference

[16] The original 60 m TIR data were used in conjunction with VI-derived model variables at 60 m to create 60 m flux maps, which were then aggregated to 120, and 240 m. These maps were used as a reference to which the other methods were compared.

#### 2.3.3.2. TsHARP

[17] The coarse (960 m) temperature fields were sharpened to 60, 120, and 240 m using the above described sharpening algorithm (section 2.1). The TSM was executed at these three finer TIR resolutions to create flux maps at 60, 120 and 240 m.

#### 2.3.3.3. UniFlux

[18] The coarse resolution TIR data were utilized by the TSM to generate 960 m flux maps. These coarse resolution fluxes were then uniformly resampled to the finer resolution grids to create flux maps at 60, 120, and 240 m. These maps serve as a baseline for assessing the improvement in spatial

information content achieved by sharpening the input thermal imagery.

## 3. Results and Discussion

[19] Previous studies have demonstrated that TsHARP, applied to 1-km thermal imagery, provided reasonably accurate finer resolution TIR maps for the WCW region [Agam *et al.*, 2007a], and to a lesser extent to the THP region [Agam *et al.*, 2007b]. Table 1 provides statistics assessing the impact of TIR sharpening on the resulting flux evaluations over these two sites, comparing maps generated with the reference, TsHARP and uniFlux techniques at each of the target resolutions.

[20] For both sites, the Mean Absolute Errors (MAE) in net radiation (Rn) and soil heat flux (G) in the TsHARP and uniFlux maps are relatively small in comparison with the errors in latent (LE) and sensible (H) heat (Table 1). Nevertheless, use of sharpened TIR inputs significantly reduced MAEs in Rn and G in comparison with the uniFlux results. This enhancement in subpixel agreement is also evidenced in the scatterplot comparisons in Figure 1, demonstrating model performance at 240 m resolution. The large improvement in Rn and particularly G as a result of sharpening reflects the fact that the TSM representation of these fluxes is strongly dependent on the assumed leaf

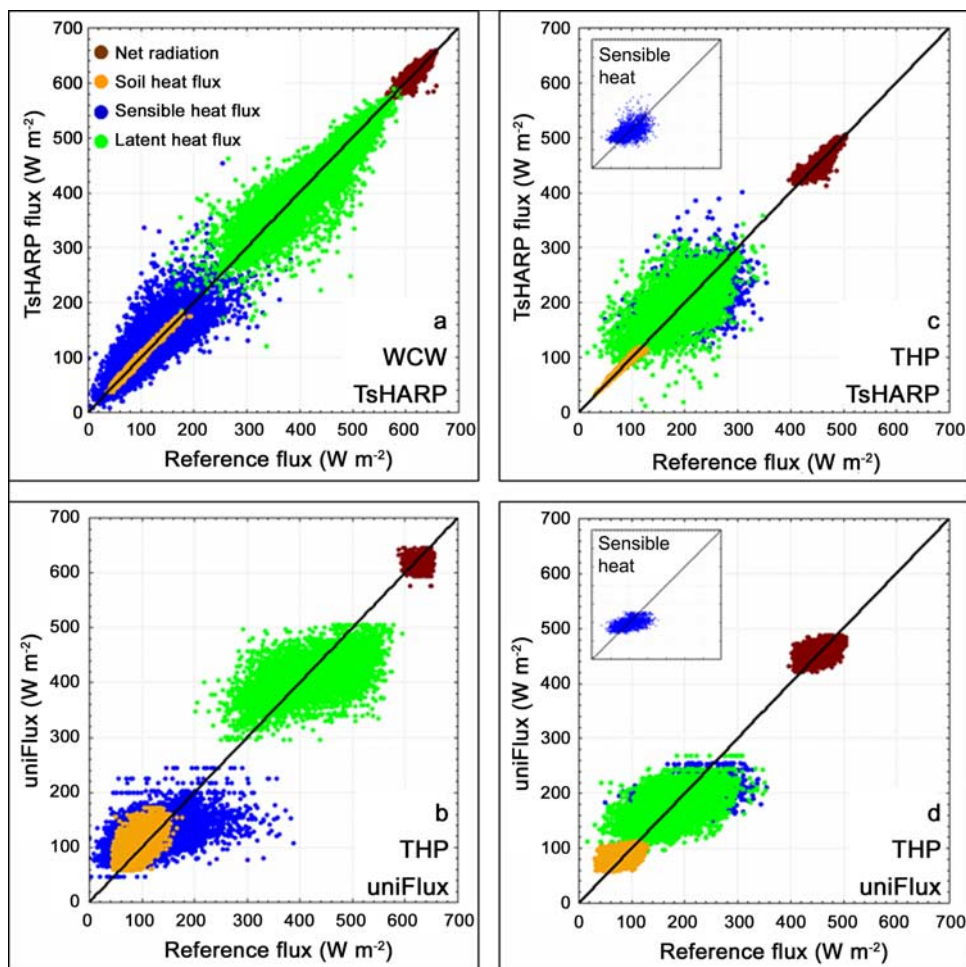


**Figure 1.** Energy balance components derived by the TSM using uniFlux and TsHARP inputs are plotted versus those derived by the reference method at 240 m, for (a) and (b) the Walnut Creek Watershed (rainfed agriculture) and (c) and (d) the Texas High Plains (irrigated agriculture) study sites. The inserts in Figures 1c and 1d are sensible heat flux and have the same axis titles and magnitudes as the panels.

area index, which is captured at the fine scale in the TsHARP results.

[21] In contrast, the use of sharpened thermal inputs to the TSM produced inconsistent results between the two sites in estimating fine-resolution H and LE. For the THP, the sharpened thermal imagery only marginally improved TSM-derived H and LE compared to the uniFlux approach. However, applying TsHARP over the WCW region reduced errors in H and LE estimation at the finer resolutions by 30–60% and significantly increased the correlations with the reference fields (Table 1 and Figure 1).

[22] The absolute magnitudes of the flux errors cannot be readily compared between the two sites due to marked differences in climatic conditions between the two imaging dates. The mean available energy ( $\langle R_n \rangle - \langle G \rangle$ , brackets represent the area-mean flux) was  $530 \text{ W m}^{-2}$  in WCW and only  $367 \text{ W m}^{-2}$  in THP, while the mean Bowen ratio ( $\langle \beta \rangle = \langle H \rangle / \langle LE \rangle$ ) was 0.32 and 1.15 for WCW and THP, respectively. Together, these factors result in largely different distributions in reference evaporation rate for the two scenes, with  $\langle LE \rangle \sim 400 \pm 48 \text{ W m}^{-2}$  for WCW versus  $\langle LE \rangle \sim 170 \pm 32 \text{ W m}^{-2}$  for THP (Table 1). Measures of correlation

provide a more meaningful basis for comparison, reflecting the ability of the sharpening technique to accurately capture the range in ET present within each scene. Based on the linear regression coefficients in Table 1, it is clear that sharpening more effectively improved correlations in H and LE with respect to reference fluxes at WCW, improving  $R^2$  by a factor of  $\sim 2.5$  at WCW and only 1–1.5 at THP.

[23] The performance of TsHARP in terms of flux evaluations over these agricultural regions can be assessed visually by comparing the 60 m resolution maps of LE shown in Figure 2. The sharpened thermal images better reproduce the full range in ET in the reference field for the WCW site than for the THP site. In addition, the THP maps suffer from the same “box-like” features that were identified by *Agam et al.* [2007b] in the sharpened TIR images, associated with the reintroduction of the residuals determined at the coarse scale to the TIR-VI sharpening relationship. In contrast, these coarse-scale artifacts were not evident in the sharpened TIR fields for WCW [*Agam et al.*, 2007a], nor do they appear in the derived ET maps.

[24] The difference in the performance of the sharpening algorithm in estimating ET over these two sites is due

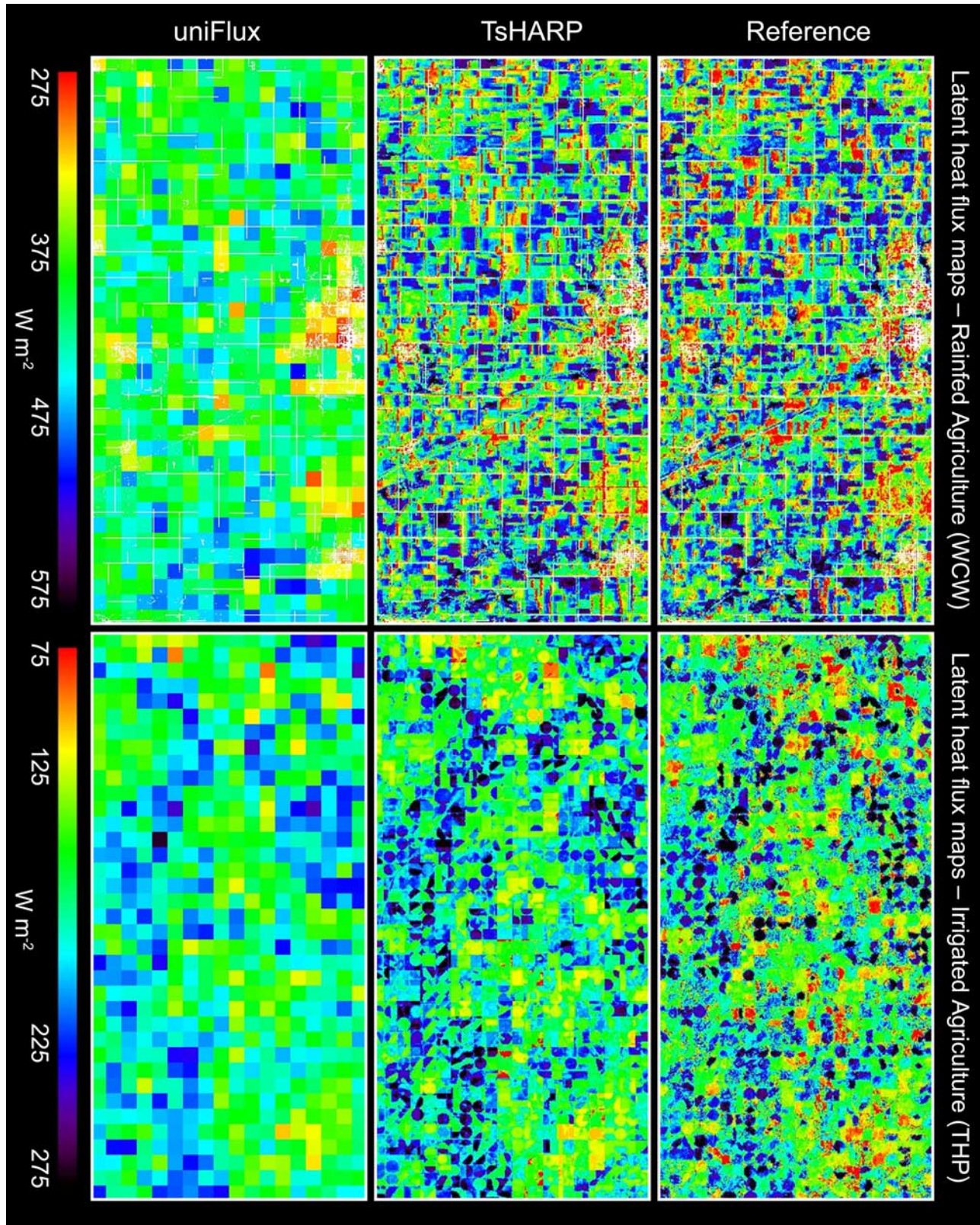


**Figure 2.** Latent heat flux maps at 60 m spatial resolution derived by the TSM, using the reference, TsHARP, and uniFlux methods, for the WCW (rainfed agriculture) and THP (irrigated agriculture) study sites. The white areas in the WCW maps mask urban pixels, for which fluxes were not computed.

primarily to the spatial scale of moisture variability associated with rainfed and irrigated agriculture. Land surface temperature is driven by several factors, but the main contributors are the fractional vegetation cover (with higher cover fraction typically associated with lower temperature) and the soil moisture content (with moister soil having lower temperature). The sharpening algorithm captures the relationship between vegetation cover amount and surface temperature, but cannot account for soil moisture variations except at the coarse native TIR resolution. For irrigated agricultural regions, soil moisture variations are often at field and sub-field scales (adjacent farms may be irrigated on different schedules, and at times, irrigation is applied only to portions of fields), thus water stress conditions are likely to develop locally. The sharpening technique is unable to detect these sub-thermal-pixel areas of stress (low LE), as illustrated by Figure 2. The soil moisture in rainfed agricultural regions, on the other hand, is largely determined by the spatial extent of precipitation events, which typically cover much larger areas, often encompassing several coarse ( $\sim 1$  km) pixels. Consequently, water stress conditions are likely to develop over larger areas and can therefore be accounted for in the sharpened temperature fields.

[25] Note that the irrigated THP landscape in Figure 2 exhibits stronger spatial structure at the 1-km (unsharpened) scale than does the WCW scene. This large-scale structural component may be contributing to the lower flux errors in the uniFlux maps over the THP, but it cannot be concluded that 1-km imagery is therefore sufficient for ET evaluations over this kind of domain. Based on field-average ET  $\langle LE_{\text{field}} \rangle$  estimates drawn from a random sample of 30 fields in each scene, the sharpened  $\langle LE_{\text{field}} \rangle$  reproduces the reference flux values from WCW with 10% for 83% of the fields. In the THP scene, only 40% of the fields are within 10% of the reference values, with errors for 2 of the fields (7%) exceeding 150% and significant biases on both the wet and dry ends of the sampled ET range. For crop water use and stress monitoring on a pivot-by-pivot basis, such errors at the field scale would be deemed unacceptable. Therefore, reliable monitoring of ET using thermal-based techniques over this type of irrigated landscape requires thermal imagery at finer native resolutions (i.e.,  $< 100$  m).

#### 4. Conclusions

[26] In the absence of satellite systems providing fine resolution ( $< 100$  m) thermal satellite data with frequent (every few days) revisit times, TsHARP provides a valuable tool for monitoring ET at field scales over the Walnut Creek Watershed, representing rainfed agricultural areas. In contrast, over the Texas High Plains, representing irrigated agricultural regions, TIR data sharpened from 1 km resolution and used by the TSM are unable to produce accurate high resolution ET maps due to sub-pixel variability in moisture patterns that are not captured by the thermal sharpening algorithm. Consequently, for precision management and decision support systems designed for irrigated agricultural areas, there is still a need for high resolution ( $< 100$  m) thermal imagery in order to provide important field-scale crop water use information.

[27] While further study is required to generalize these conclusions, the results from these two sites are likely to be representative of typical rainfed and irrigated agricultural regions during the growing season when such information would improve water management decisions.

[28] **Acknowledgments.** This research was supported by Vaadia-BARD Postdoctoral Fellowship Award FI-371-2005 from BARD, United States–Israel Binational Agricultural Research and Development Fund.

#### References

- Agam, N., W. P. Kustas, M. C. Anderson, F. Li, and C. M. U. Neale (2007a), A vegetation index based technique for spatial sharpening of thermal imagery, *Remote Sens. Environ.*, *107*, 545–558.
- Agam, N., W. P. Kustas, M. C. Anderson, F. Li, and P. D. Colaizzi (2007b), Utility of thermal sharpening over Texas high plains irrigated agricultural fields, *J. Geophys. Res.*, *112*, D19110, doi:10.1029/2007JD008407.
- Anderson, M. C., C. M. U. Neale, F. Li, J. M. Norman, W. P. Kustas, H. Jayanthi, and J. Chavez (2004), Upscaling ground observations of vegetation water content, canopy height, and leaf area index during SMEX02 using aircraft and Landsat imagery, *Remote Sens. Environ.*, *92*, 447–464.
- Anderson, M. C., J. M. Norman, J. R. Mecikalski, J. A. Otkin, and W. P. Kustas (2007), A climatological study of evapotranspiration and moisture stress across the continental United States based on thermal remote sensing: 1. Model formulation, *J. Geophys. Res.*, *112*, D10117, doi:10.1029/2006JD007506.
- Becker, F., and Z.-L. Li (1990), Temperature-independent spectral indices in thermal infrared bands, *Remote Sens. Environ.*, *32*, 17–33.
- Berk, A., L. S. Bernstein, G. P. Anderson, P. K. Acharya, D. C. Robertson, J. H. Chetwynd, and S. M. Adler-Golden (1998), MODTRAN cloud and multiple scattering upgrades with application to AVIRIS, *Remote Sens. Environ.*, *65*, 367–375.
- Colaizzi, P. D., P. H. Gowda, T. H. Marek, and D. O. Porter (2006), Reducing Ogallala withdrawals by changing cropping and irrigation practices in the Texas high plains, paper presented at Ground Water and Surface Water Under Stress: Competition, Interaction, Solutions, U.S. Comm. on Irrig. and Drain., Boise, Idaho.
- Diak, G. R., J. R. Mecikalski, M. C. Anderson, J. M. Norman, W. P. Kustas, R. D. Torn, and R. L. DeWolf (2004), Estimating land-surface energy budgets from space: Review and current efforts at the University of Wisconsin-Madison and USDA-ARS, *Bull. Am. Meteorol. Soc.*, *85*, 65–78.
- Doraiswamy, P. C., J. L. Hatfield, T. J. Jackson, B. Akhmedoc, J. Prueger, and A. Stern (2004), Crop condition and yield simulations using Landsat and MODIS, *Remote Sens. Environ.*, *92*, 548–559.
- Hatfield, J. L., J. H. Prueger, and D. W. Meek (1999), Spatial variation of rainfall over a large watershed in central Iowa, *Theor. Appl. Climatol.*, *64*, 49–60.
- Homer, C., C. Huang, L. Yang, B. Wylie, and M. Coan (2004), Development of a 2001 national land-cover database for the United States, *Photogramm. Eng. Remote Sens.*, *70*, 829–840.
- Kustas, W. P., and J. M. Norman (1999a), Evaluation of soil and vegetation heat flux predictions using a simple two-source model with radiometric temperatures for partial canopy cover, *Agric. For. Meteorol.*, *94*, 13–25.
- Kustas, W. P., and J. M. Norman (1999b), Reply to comments about the basic equations of dual-source vegetation-atmosphere transfer models, *Agric. For. Meteorol.*, *94*, 275–278.
- Kustas, W. P., and J. M. Norman (2000), A two-source energy balance approach using directional radiometric temperature observations for sparse canopy covered surfaces, *Agron. J.*, *92*, 847–854.
- Kustas, W. P., J. M. Norman, M. C. Anderson, and A. N. French (2003), Estimating subpixel surface temperatures and energy fluxes from the vegetation index-radiometric temperature relationship, *Remote Sens. Environ.*, *85*, 429–440.
- Kustas, W. P., J. Hatfield, and J. H. Prueger (2005), The Soil Moisture Atmosphere Coupling Experiment (SMACEX): Background, hydrometeorological conditions and preliminary findings, *J. Hydrometeorol.*, *6*, 791–804.
- Li, F., T. J. Jackson, W. P. Kustas, T. J. Schmugge, A. N. French, M. Cosh, and R. Bindlish (2004), Deriving land surface temperature from Landsat 5 and 7 during SMEX02/SMACEX, *Remote Sens. Environ.*, *92*, 521–534.
- Nishida, K., R. R. Nemani, J. M. Glassy, and S. W. Running (2003), Development of an evapotranspiration index from Aqua/MODIS for monitoring surface moisture status, *IEEE Trans. Geosci. Remote Sens.*, *41*, 493–501.

- Norman, J. M., and F. Becker (1995), Terminology in thermal infrared remote sensing of natural surfaces, *Agric. For. Meteorol.*, 77, 153–166.
- Norman, J. M., W. P. Kustas, and K. S. Humes (1995), Source approach for estimating soil and vegetation energy fluxes from observations of directional radiometric surface temperature, *Agric. For. Meteorol.*, 77, 263–293.
- Sobrinho, J. A., N. Raissouni, and Z.-L. Li (2001), A comparative study of land surface emissivity retrieval from NOAA data, *Remote Sens. Environ.*, 75, 256–266.
- 
- N. Agam, M. C. Anderson, W. P. Kustas, and F. Li, USDA-ARS Hydrology and Remote Sensing Lab., Bldg. 007, BARC-West, Beltsville, MD 20705, USA. (nurit.agam@gmail.com)
- P. D. Colaizzi, Conservation and Production Research Laboratory, Agricultural Research Service, U.S. Department of Agriculture, Bushland, TX 79012–0010, USA.